

Evolution of defects and deformation mechanisms in different tensile directions of solidified lamellar Ti-Al alloy

Yutao Liu(刘玉涛), Tinghong Gao(高廷红), Yue Gao(高越), Lianxin Li(李连欣), Min Tan(谭敏),Quan Xie(谢泉), Qian Chen(陈茜), Zean Tian(田泽安),Yongchao Liang(梁永超), and Bei Wang(王蓓)

Citation: Chin. Phys. B, 2022, 31 (**4**): 046105. DOI: 10.1088/1674-1056/ac1f0b
Journal homepage: http://cpb.iphy.ac.cn; http://iopscience.iop.org/cpb

What follows is a list of articles you may be interested in

First-principles study of two new boron nitride structures: C12-BN and O16-BN

Hao Wang(王皓), Yaru Yin(殷亚茹), Xiong Yang(杨雄), Yanrui Guo(郭艳蕊), Ying Zhang(张颖), Huiyu Yan(严慧羽), Ying Wang(王莹), and Ping Huai(怀平)

Chin. Phys. B, 2022, 31 (**2**): 026102. DOI: 10.1088/1674-1056/ac0a69

Polymorph selection of magnesium under different pressures: A simulation study

Wei Liu(刘维), Boqiang Wu(吴博强), Ze'an Tian(田泽安), Yunfei Mo(莫云飞), Tingfei Xi(奚廷斐), Zhiyi Wan(万子义), Rangsu Liu(刘让苏), and Hairong Liu(刘海蓉)

Chin. Phys. B, 2022, 31 (**1**): 016103. DOI: 10.1088/1674-1056/ac2e5e

Mechanism of microweld formation and breakage during Cu-Cu wire bonding investigated by molecular dynamics simulation

Beikang Gu(顾倍康), Shengnan Shen(申胜男), and Hui Li(李辉)

Chin. Phys. B, 2022, 31 (**1**): 016101. DOI: 10.1088/1674-1056/ac0e24

A novel two-dimensional SiO sheet with high-stability, strain tunable electronic structure, and excellent mechanical properties

Shijie Liu(刘世杰) and Hui Du(杜慧)

Chin. Phys. B, 2021, 30 (**7**): 076104. DOI: 10.1088/1674-1056/abf34d

Non-monotonic temperature evolution of nonlocal structure-dynamics correlation in CuZr glass-forming liquids

W J Jiang(江文杰) and M Z Li(李茂枝)

Chin. Phys. B, 2021, 30 (**7**): 076102. DOI: 10.1088/1674-1056/abf113

Evolution of defects and deformation mechanisms in different tensile directions of solidified lamellar Ti–Al alloy

Yutao Liu(刘玉涛)[1], Tinghong Gao(高廷红)[1,†], Yue Gao(高越)[1], Lianxin Li(李连欣)[1], Min Tan(谭敏)[1], Quan Xie(谢泉)[1], Qian Chen(陈茜)[1], Zean Tian(田泽安)[1,2], Yongchao Liang(梁永超)[1], and Bei Wang(王蓓)[1]

[1] *Institute of New Optoelectronic Materials and Technology, College of Big Data and Information Engineering, Guizhou University, Guiyang* 550025, *China*
[2] *College of Computer Science and Electronic Engineering, Hunan University, Changsha* 410082, *China*

(Received 3 July 2021; revised manuscript received 10 August 2021; accepted manuscript online 19 August 2021)

Two-phase γ-TiAl/α_2-Ti_3Al lamellar intermetallics have attracted considerable attention because of their excellent strength and plasticity. However, the exact deformation mechanisms remain to be investigated. In this paper, a solidified lamellar Ti–Al alloy with lamellar orientation at 0°, 17°, and 73° with respect to the loading direction was stretched by utilizing molecular dynamics (MD) simulations. The results show that the mechanical properties of the sample are considerably influenced by solidified defects and tensile directions. The structure deformation and fracture were primarily attributed to an intrinsic stacking fault (ISF) accompanied by the nucleated Shockley dislocation, and the adjacent extrinsic stacking fault (ESF) and ISF formed by solidification tend to form large HCP structures during the tensile process loading at 73°. Moreover, cleavage cracking easily occurs on the γ/α_2 interface under tensile deformation. The fracture loading mechanism at 17° is grain boundary slide whereas, at 73° and 0° , the dislocation piles up to form a dislocation junction.

Keywords: molecular dynamics simulation, solidified lamellar Ti–Al alloy, tensile directions, γ/α_2 interface

PACS: 61.72.Ff, 83.50.–v, 81.40.Lm, 31.15.xv **DOI:** 10.1088/1674-1056/ac1f0b

1. Introduction

The Ti–Al-based alloy is a promising candidate to replace Ni-based superalloys in the automotive and aerospace industries. This is mainly attributed to its low density, high strength retention, high specific strength, and high creep resistance.[1,2] However, the primary concerns with single-crystalline and polycrystalline Ti–Al alloys are their low yield strength and poor ductility at room temperature.[3] Recently, Ti–Al alloys were formed entirely from lamellar colonies composed of γ-TiAl and α_2-Ti_3Al, which exhibit excellent ductility and strength across a wide range of temperatures.[4,5]

In the two-phase lamellar Ti–Al alloy (γ-TiAl with an $L1_0$ type of face-centered cubic (FCC) structure while α_2-Ti_3Al with a DO_{19} type of hexagonal close-packed (HCP) structure), the interface between different phases can be either γ/α_2 or γ/γ, and their orientation always follows the Blackburn relationship, $(111)\gamma//(0001)\alpha_2$, $[1\text{-}10]\gamma//\langle 11\text{-}20\rangle\alpha_2$.[6] In previous studies, the plastic deformation of lamellar Ti–Al alloy mainly appeared in the γ-TiAl phase because the number of slip systems is greater than the α_2-Ti_3Al phase and the quite considerable hardness of α_2-Ti_3Al.[7,8] The γ-TiAl has three major competing deformation modes: $1/2\langle 110]$ ordinary dislocation, $\langle 101]$ superlattice dislocation and $\{111\}\langle 11\text{-}2]$ true twin.[9] These deformation modes strongly depend on orientation due to both the unidirectional nature of twinning and the polarization of superlattice dislocation.[10] Therefore, the two-phase Ti–Al alloy shows strongly anisotropic mechanical properties. Chen *et al.*[11] successfully prepared lamellar Ti–Al alloy using a directional solidification method and investigated its mechanical properties. They reported that the sample's yield strength with 0° lamellar orientation exceeded 45°. Palomares-García *et al.*[12] examined the deformation mechanisms of lamellar Ti–Al alloy with lamellae oriented at 0°, 45°, and 90° to the compress direction. Their results uncovered a large plastic anisotropy. Moreover, Pan *et al.*[13] reported that when the nanotwins were tilted at 15° of the deformation axis, a necklace-type of dislocation could be produced, which helps to maintain the structure's stability. Hence, it is important to understand the deformation direction effect on the mechanical properties of lamellar Ti–Al alloys.

However, experimental deformation tests are tedious, expensive, and hard to directly observe at the atomic scale. In recent years, several studies have shown that molecular dynamics (MD) simulation is an effective tool that can provide physical insights into the understanding of the deformation behavior of materials at an atomic level and can enable one to predict the mechanical properties.[8,14–16] But in these research studies, lamellar samples were created artificially, such as by using the Atomsk software based on Voronoi tessellation methods. Nevertheless, in the initial configuration there is dislocation at the γ/α_2 interface because of the lattice mismatch. Furthermore, solidification plays an important role in metal processing, such as casting and additive manufacturing. The structure after solidification is distinctly different from single

†Corresponding author. E-mail: gaotinghong@sina.com
© 2022 Chinese Physical Society and IOP Publishing Ltd

crystal counterparts. In high-performance materials, the study of the defects' evolution and the mechanical response of materials at the nanoscale on deformation is important.

To better understand the influence of solidified defects on the tensile response, in this work, based on MD simulation, we apply a rapid solidification method with a cooling rate of 0.01 K/ps to produce a lamellar Ti–Al alloy sample. The influences of the X-, Y-, and Z-axes under three different tensile directions on the sample, the evolution of defects, and structure deformation mechanisms are investigated.

2. Simulation method

MD simulations of rapid solidification and deformation of solidified Ti–Al alloy processes were conducted using a simulation box comprising 32000 atoms (24000 Ti and 8000 Al atoms). The EAM potential was adopted to model the interatomic of the Ti–Al system since it was extensively used to simulate the rapid solidification and deformation process, and the results agree well with the experimental data.[17–20] We utilized 3D periodic boundary conditions and an invariant timestep of 0.001 ps.

First, the solidification simulation was conducted under constant pressure and constant temperature (NPT ensemble) using the Nose–Hoover thermostat and Parrinello–Rahman method to control the temperature and vacuum. Before quenching, we obtained the equilibrium liquid by relaxing the system for 100 ps at 2000 K (higher than the experimental melting point of Ti–Al alloy).[21] Then, the system was cooled down to 200 K with a cooling rate of 0.01 K/ps. Second, the solidified sample was deformed in tension by a straining box at a strain rate of 2×10^9 s^{-1} along the X-, Y-, and Z-axes at 200 K under a canonical (NVT) ensemble by running for 200 ps, respectively. For visualization and defect analysis purposes, the open visualization tool (OVITO) together with common neighbor analysis (CNA)[22] and dislocation extraction algorithm (DXA) commands[23] were used.

3. Results and discussion

3.1. Solidified lamellar sample

Figure 1(a) shows the solidified Ti–Al lamellar sample. It can be seen that the sample consists of an FCC phase separated by a HCP phase, an extrinsic stacking fault (ESF), an intrinsic stacking fault (ISF), and a twin (the ESF, ISF, and the twin correspond to 3, 2, and 1 in Fig. 1(d), respectively). To identify the structure type, the simulated powder x-ray diffraction pattern (XRD) was adopted and the conclusion is shown in Fig. 1(b). According to the experiment and simulation XRD peaks,[24,25] we find that the structure consists of γ-TiAl + α_2-Ti_3Al. Note that, because of the limited simulation size, the strength and width of the XRD peaks cannot be directly compared with the experimental data. Under non-equilibrium rapid solidification conditions, the sample could be defective and could have dislocation lines and voids distribution, as shown in Fig. 1(c). Interestingly, multiple dislocation lines intersect with each other to form a dislocation junction located at the grain boundary (the black circle in Fig. 1(c)). From it, we can see the dislocation lines are dominated by Shockley dislocation and its distribution along the grain boundary. Figures 1(d)–1(f) show the view from the X-, Y-, and Z-axes, and the tensile angles along the X-, Y-, and Z-axes with the γ/α_2 interface are about 17°, 73°, and 0°, respectively (Fig. 1(d)). Continuous other atoms that form the grain boundary are found in Fig. 1(f).

3.2. Different responses of the structure under three loading directions

In Fig. 2, the stress–strain curves, number of crystal structural types, and dislocation density behavior have been employed to explore the effect of orientation simulations with tensile loading along the X-, Y-, and Z-axes. Before the material failure, the process of tensile deformation can be divided into elastic deformation (stage I), the yield stage (stage II), and the work hardening stage (stage III) (Figs. 2(a)–2(c)). In the elastic deformation stage (I), the relationship between stress and strain increases linearly until points a, d, and g along the X-, Y-, and Z-axes, respectively, which agrees with the results of the theoretical Hooke's law. At this stage, the lamellar Ti–Al alloy will return to its original configuration if the load is removed. With the increase in tensile strain, the sample begins to enter the yield stage (II), and the linear relationship between stress and strain is broken. When the strain surpasses points b, e, and h, the stress continues to increase with the strain during the working hardening stage. The points c, f, and i are the maximum strain before material fracture; then, the stress experienced a sharp decrease. The tensile response of the three loading directions exhibits strong anisotropy, and the stress–strain curves of the tensile response along the Y- and Z-directions drop slightly to points e and h, respectively, which is the so-called yield point. However, no significant yield point was found in the X-direction stretching process. Thus, according to Fig. 1(d), showing the strain corresponding to the maximum value of HCP atoms, we mark point b in Fig. 1(a) as the yield point of the X-direction. Table 1 shows the strain and stress of nine points and elastic modulus of three directions. It is obvious that the critical strength and elongation along the X-direction are the highest but the elastic modulus is smaller than Y and Z. The elastic modulus of the Ti–Al alloy in experimental data is about 120–140 GPa,[26] demonstrating that the simulation results are in excellent agreement with experimental values.

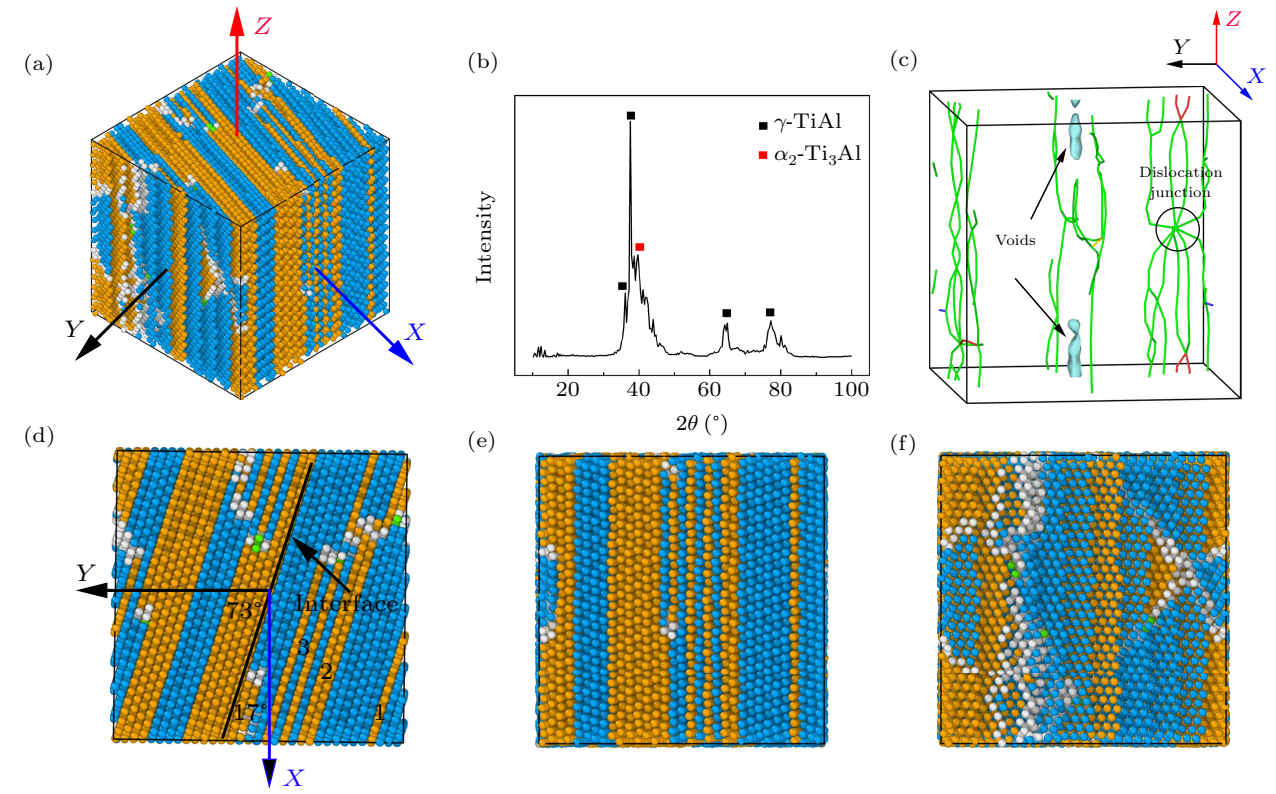


Fig. 1. A schematic of the initial solidified lamellar sample. (a) An overall view of the sample. (b) The XRD pattern. (c) Dislocation lines and voids distribution. The winered, blue, green, red, and yellow lines represent the other, perfect, Shockley, stair-rod, and Hirth dislocations, respectively. The cyan surface was colored according to DXA defect mesh. (d), (e) and (f) are the views from the *X*-, *Y*-, and *Z*-axes, respectively. Atoms are colored based on their spatial coordinates of the DXA algorithm: blue→FCC, yellow→HCP, green→BCC, and white→other.

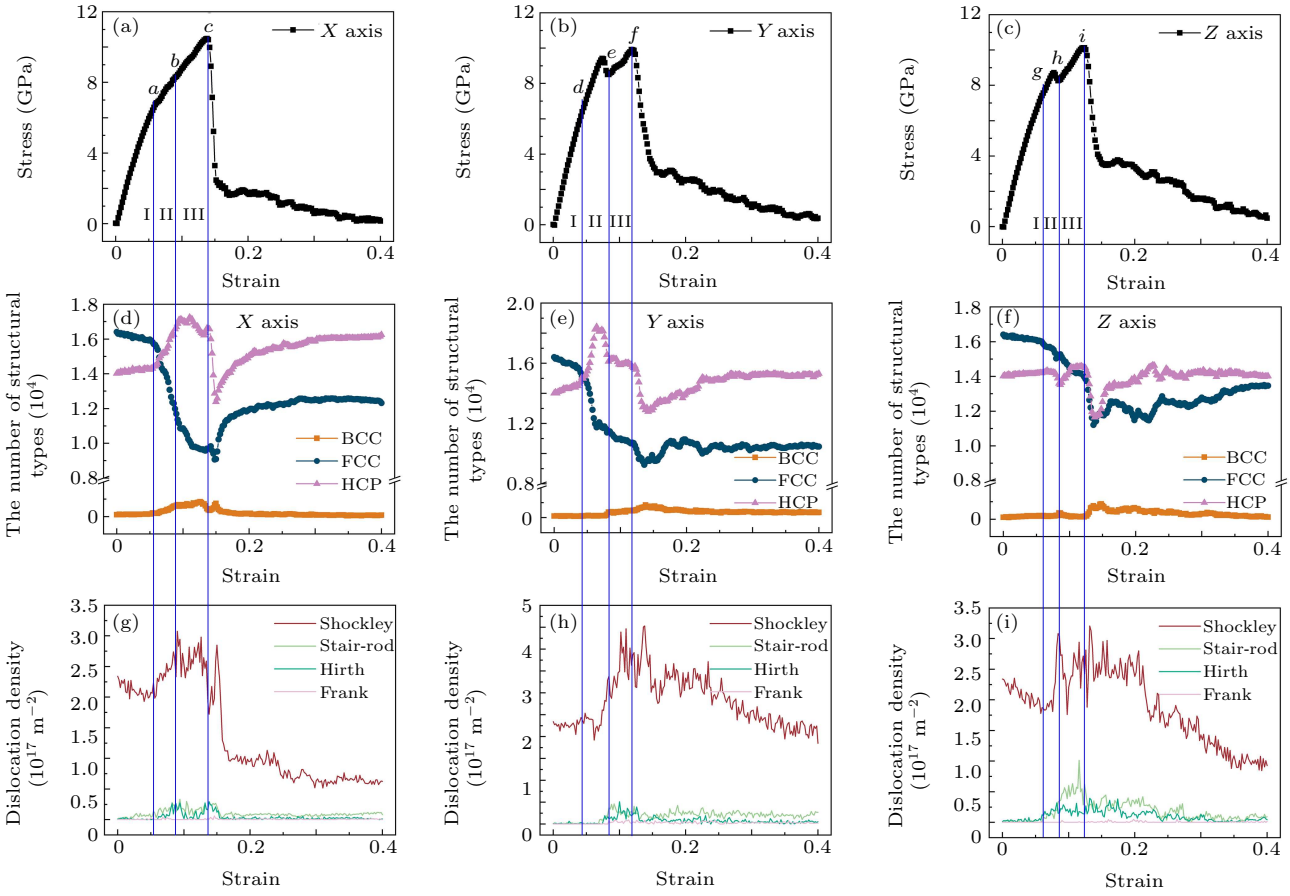


Fig. 2. (a)–(c) Tensile stress–strain curves, (d)–(f) the number of crystal structural types, and (g)–(i) dislocation densities as a function of strain for the *X*-, *Y*-, and *Z*-axes, respectively.

Table 1. Physical parameters of nine points. The maximum strain and stress under three loading directions are indicated in bold.

Direction		X			Y			Z	
Point	a	b	c	d	e	f	g	h	i
Strain	0.062	0.09	**0.138**	0.048	0.082	**0.118**	0.064	0.088	**0.122**
Stress (GPa)	6.83	8.23	**10.48**	6.87	8.50	**9.92**	7.21	8.34	**10.14**
Elastic modulus (GPa)		110			143			120	

Understanding the variation of crystal structural types during the tensile process is of great significance when determining the evolution of a microstructure. Figures 2(d)–2(f) show the evolution of structure types in the X-, Y-, and Z-axes during the stretching process. The variation trend of HCP atoms in the three directions is somewhat different, while the number of FCC atoms decreases all the time before the whole breaking. In stage I, the number of HCP atoms experiences a small increase in three directions. After this, the material enters stage II, and the HCP atoms undergo a rapid increase in the X- and Y-directions, reaching a maximum in the X-direction but decreasing rapidly after reaching a maximum in the Y-direction. However, the HCP atoms in the Z-direction increase slightly and then decrease. During stage III, the number of HCP atoms in the X- and Y-axes drops slightly, but the HCP atoms' tensile response along with the Z-axis rises and then remains unchanged. It is well known that the γ-TiAl is much softer than the α_2-Ti_3Al, so the number of HCP atoms increases because of the dislocation movement during plastic deformation caused by stacking faults and grain boundary defects formed by HCP in the γ-TiAl phase. Therefore, the structural changes may be obvious when observed together with X- and Y-direction deformation. The FCC and HCP atoms are increased after tensile fracture due to stress relaxation accompanied by strain microstructure recovery.[18] Few BCC atoms will be formed during the tensile process, and the number is too small to wildly fluctuate during the stretching process.

Figures 2(g)–2(i) show the densities of Shockley, stair-rod, Hirth, and Frank dislocation evolution. The Shockley dislocation is almost dominant in the system, while the Frank dislocation always zeroes. In the elastic deformation stage I, the Shockley dislocation slowly decreases in the X- and Z-directions while, in the Y-direction, it should slightly fluctuate. When the strain enters stage II, the Shockley dislocation monotonically increases as the strain increases. At stage III, the Shockley dislocation experiences complex variation. However, after the strain surpasses points c, f, and i, the Shockley dislocation experiences a jump-up and then drop-off in three directions and a subsequent decrease in volatility. This trend indicates that the fracture of the alloy is attributed to the nucleated Shockley dislocation. The stair-rod and Hirth dislocations after stage I have a modest increase then continue fluctuating. Interestingly, the stair-rod dislocation in the Z-direction has a sudden increase then a drop followed by eventual maintenance of a small number of fluctuations (Fig. 2(i)). The stair-rod dislocation as a motionless dislocation has a significant effect on material enhancement.[27] Therefore, the slope of the strain–stress curve in the Z-direction is greater than in the other two at stage III.

Define Φ as the angle between the tensile direction of the lamellar boundaries. In general, the yield strength and ductility depend on Φ. The lamellar crystal exhibits the highest strength but low ductility when $\Phi = 90^\circ$. There is a good balance between ductility and strength at $\Phi = 0^\circ$, where the strength is not as high as for $\Phi = 90^\circ$ but ductility is large at 5%–10%.[28] But $\Phi = 17^\circ$, 73°, 0° corresponds to the X-, Y-, and Z-axes in this paper, respectively. However, the ductility and strength of $\Phi = 17^\circ$ are higher than the other two. This is because the lamellar structural lattice obtained by solidification herein is imperfect and defective. The defects formed by solidification may considerably influence the deformation of materials.

3.3. Analysis of microstructure evolution

To further investigate the deformation behavior of tensile loading along the X-, Y-, and Z-axes from an atomic viewpoint, snapshots of microstructure evolution in solidified samples at nine points are listed in Fig. 3. The atoms are colored using the DXA algorithm. When the tensile direction is along the X-axis, it is found that the Shockley dislocation begins to nucleate at $\varepsilon_a = 0.062$ (in the circle, the arrow represents the direction of dislocation motion). As the strain increases to $\varepsilon_b = 0.09$, the system appears to have ISFs that are parallel to each other. Furthermore, the ESF is transformed into ISFs along the direction of the black arrow (inside the rectangular box), and it is also accompanied by a Shockley dislocation. At $\varepsilon_c = 0.138$, mutually parallel ISFs and from those ESFs that have transformed into ISFs intersect to form junctions. Simultaneously, in the deformation zone of γ-TiAl, there are only a few dislocation lines; however, in the tensile direction of the Y-axis, the ISF first nucleates beside the ISF formed by initial solidification at $\varepsilon_d = 0.048$ and then moves along the black arrow direction. When the strain increases to $\varepsilon_e = 0.082$, the part of the ESF begins to transform into the HCP phase. At the critical strain of $\varepsilon_f = 0.118$, the structure of the system began to produce major disruptions, and the Shockley dislocation nucleated again. At this point, the bulk of the HCP phase has formed at the original ISF and ESF positions; the tensile along

the Z-axis, in which the structure has not changed too much, is quite different from the X-, and Y-axes. At $\varepsilon_g = 0.064$, the Shockley dislocation first formation in the FCC phase then spreads toward the HCP phase. Before material fracture, the ISFs have been formed across the HCP phase with Shockley dislocation.

In brief, regardless of the tensile direction, ISFs are mainly formed accompanied by the Shockley dislocation. In addition, ISFs were formed that intersect each other in the X-direction, indicating that only a single slip system with a slip plane was active during the deformation process, except for the stacking defects evolution. However, when stretching along the Y-direction, the pre-existing ISF and ESF formed a large HCP structure in the case of tensile deformation; therefore, the phase transition of FCC to HCP occurred in the tensile direction of Y. The structure of the system does not change much, except for the movement of dislocations before the alloy fracture.

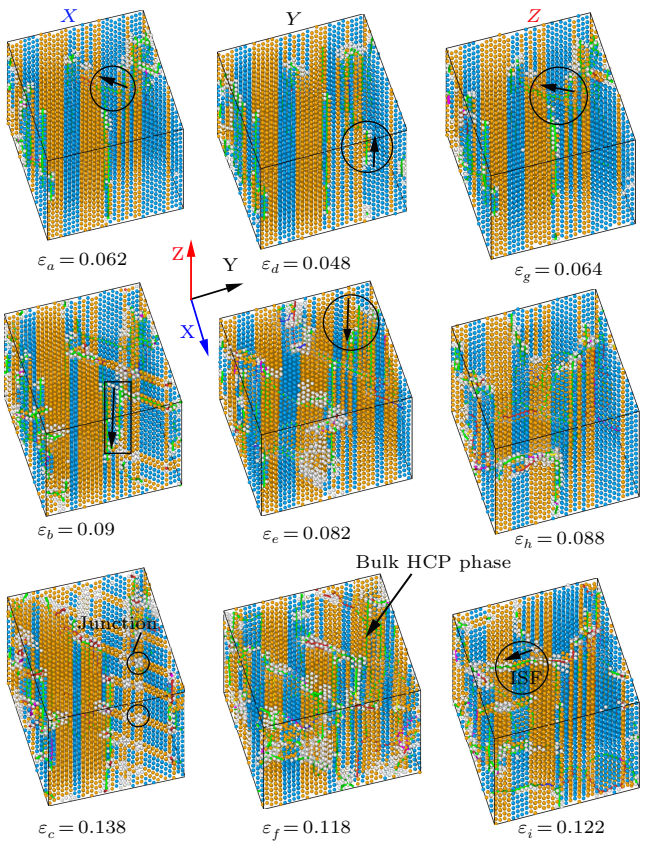


Fig. 3. Evolution of the solidified sample structure during tensile deformation. Atoms are colored by the DXA algorithm, and blue, yellow, green, and white represent FCC, HCP, BCC, and other atoms, respectively. The winered, blue, green, red, and yellow lines represent the other, perfect, Shockley, stair-rod, and Hirth dislocations, respectively.

3.4. The sample fracture mechanism

The dislocation motion remarkably during the tensile process. According to Fig. 3, the $\varepsilon_c = 0.138$, $\varepsilon_f = 0.118$, and $\varepsilon_i = 0.122$ are the maximum critical strains under deformation along the X, Y, and Z directions, respectively. To determine the effect of atomic movement on the structure, the atomic displacement distribution map of maximum strain before material fracture of the three directions has been drawn in Fig. 4. We can see the movement of atoms leads to delamination of the structure. The atomic displacement not only moves along the dislocation motion direction but also along with the interface of the γ/α_2 phase. Therefore, cleavage cracking may easily occur on the γ/α_2 interface.

In addition, when deformation occurs along the X-axis, the system forms intersecting ISFs, indicating that atomic motions are easily carried out in this direction. The intersecting ISFs enhance the stability of the structure during tensile, which leads to the best plasticity and strength in the X-direction. When it is tensile in the Y-direction, the FCC phases in the ESF and ISF regions are transformed into the HCP phase, so the atomic motion is hindered due to the less-slip system in the HCP phase, resulting in less plasticity than in the other two directions.

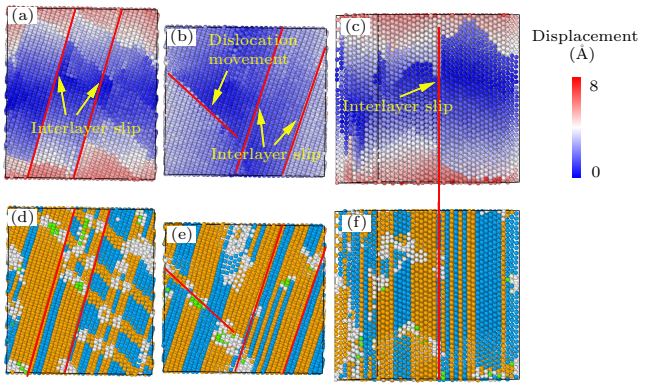


Fig. 4. The atomic structure corresponding to the maximum strain points in the three directions. (a) and (d) The structures at $\varepsilon_c = 0.138$. (b) and (e) The structures at $\varepsilon_f = 0.118$. (c) and (f) The structures at $\varepsilon_i = 0.122$. (a)–(c) Atoms are colored by displacement results. (d)–(f) Atoms are colored by the CNA algorithm. Blue, yellow, green, and white represent FCC, HCP, BCC, and Other atoms, respectively.

3.5. Evolution of dislocation and voids

In the lamellar structure of γ-TiAl/α_2-Ti_3Al, α_2-Ti_3Al with the HCP structure is the harder phase, whereas γ-TiAl with the FCC structure is the softer phase. Hence, if the lamellar sample has a perfect lattice of γ-TiAl/α_2-Ti_3Al, the microvoids, or cracks, prefer forms in the Ti_3Al lamellae.[8] However, if the lamellar sample has dislocation, voids and a grain boundary in the alloy initially, the failure mode may considerably differ. In particular, the maximum stresses of the γ/α_2 system along the X-, Y-, and Z-axes are 0.138, 0.118, and 0.122, respectively. As shown in Fig. 5, under loading along the X-axis, although there are some voids in the structure while the crack nucleates in the dislocation junction located at the grain boundary by solidification (Fig. 1(c)), the dislocation lines at the γ/α_2 interface intersect to form a new dislocation junction. However, no accumulation of dislocation lines was found at grain boundaries. With the increase

in strain, the crack continued to expand at the grain boundary leading to material failure. Therefore, the crack nucleation in the solidified sample cannot be attributed to the dislocation pile-up process but results from the sliding at the grain boundary, which was formed by solidification when tensile along the X-axis. The shear stresses increase rapidly during the sliding of the grain boundary and lead to the sample fracture. When the deformation loading occurs along the Y- and Z-axes, the dislocation evolution does not occur with the γ/α_2 interface but shows a random distribution. The main voids or dislocation junction nucleation occur at the grain boundary initially, but the formation of the void and expansion at the dislocation junction position occur due to the increase in strain, so the fracture mechanism can be attributed to the dislocation pileup. According to Fig. 2(h), the density of Shockley dislocation lines is greater than Z; this may make it easy to form the dislocation junction, thereby causing the lamellar sample failure, and the maximal stress is less than when the tensile is along the Z direction.

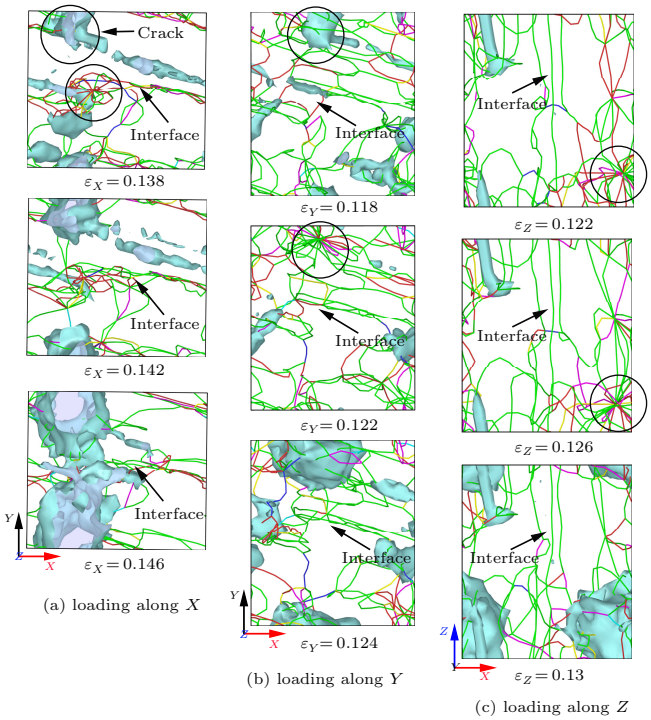


Fig. 5. Snapshots of the solidified lamellar sample at different deformation stages under three directions. The surfaces and dislocations are colored by the DXA command, and the cyan surfaces are the cracks or voids. The dislocation line's color scheme is consistent with Fig. 3.

4. Conclusion and perspectives

MD simulation utilizing the EAM potential is used to examine the evolution of defects and deformation mechanisms in different deformation directions of solidified lamellar Ti–Al alloy. The lamellar Ti–Al alloy was created by rapid solidification with a cooling rate of 0.01 K/ps. The XRD pattern demonstrates the structure consists of γ-TiAl and α_2-Ti_3Al phases. Tensile deformation of the lamellar structure along the X-, Y-, and Z-axes is observed at 17°, 73°, and 0° to the γ/α_2 interface. The following conclusions can be obtained from this study.

(i) The stress–strain behavior of the solidified γ/α_2 lamellar system shows strong anisotropy. The strength and ductility loading at 17° exceeds those at 73° and 0° because the intersecting format of ISFs enhances the structure's stability.

(ii) The mechanical properties of the sample are strongly influenced by solidified defects. The structure deformation and fracture occurred primarily via ISFs accompanied by the nucleated Shockley dislocation. During tensile loading at 73°, the adjacent ESF and ISF formed by solidification tend to form large HCP structures.

(iii) The plastic anisotropy of the lamellar sample is attributed to dislocation movement and localized slip of the γ/α_2 interface. Thus, for the lamellar structure under tensile deformation, cleavage cracking easily occurs on the γ/α_2 interface.

(iv) The fracture mechanism of loading at 17° is the grain boundary sliding whereas, for the loadings at 73° and 0°, the dislocation piled up to form the dislocation junction.

Acknowledgments

Project supported by the National Natural Science Foundation of China (Grant Nos. 51761004, 51661005, and 11964005), Industry and Education Combination Innovation Platform of Intelligent Manufacturing and Graduate Joint Training Base at Guizhou University (Grant No. 2020-520000-83-01-324061), the Guizhou Province Science and Technology Fund, China (Grant Nos. ZK[2021] 051, [2017] 5788, and J[2015] 2050), High Level Creative Talent in Guizhou Education Department of China, and the Cooperation Project of Science and Technology of Guizhou Province, China (Grant No. LH[2016] 7430).

References

[1] Tian Y B, Shen J Q, Hu S S, Gou J and Cui Y 2021 *J. Mater. Sci. Technol.* **74** 35
[2] Rittinghaus S K and Wilms M B 2019 *J. Alloys Compd.* **804** 457
[3] Appel F and Wagner R 1998 *Mater. Sci. Eng.* **22** 187
[4] Umer Ilyas M and Rizviul Kabir M 2021 *Intermetallics* **132** 107129
[5] Umer Ilyas M and Rizviul Kabir M 2020 *J. Mater. Sci. Eng. A* **788** 139524
[6] Mathabathe M N, Bolokang A S, Govender G, Mostert R J and Siyasiya C W 2018 *J. Alloys Compd.* **765** 690
[7] Neogia A and Janisch R 2021 *Acta Mater.* **213** 116924
[8] Li W, Yin Y J, Xu Q, Zhou J X, Nan H, Ji X Y, Shen X, Feng X, Yu W, Tu Z X and Pang N 2019 *Comput. Mater. Sci.* **159** 397
[9] Palomares-García A J, Perez-Prado MT and Molina-Aldareguia J M 2017 *Acta Mater.* **123** 102
[10] Paidar V, Kishida K and Yamaguchi M 2003 *J. Mater. Res.* **18** 702
[11] Chen G, Peng Y B, Zheng G, Qi Z X, Wang M Z, Yu H C, Dong C L and Liu C T 2016 *Nat. Mater.* **15** 876
[12] Palomares-García A J, Perez-Prado M T and Molina-Aldareguia J M 2017 *Acta Mater.* **123** 102
[13] Pan Q S, Zhou H F, Lu Q H, Gao H J and Lu L 2017 *Nature* **551** 214
[14] Li P T, Yang Y Q, Koval V, Chen J X, Luo X, Zhang W, Wang B and Yan H X 2021 *Mater. Des.* **199** 109422

[15] Han X L, Liu P, Sun D L and Wang Q 2019 *Theor. Appl. Fract. Mech.* **101** 217
[16] Zhang L, Lü C, Kiet T, Pei L Q and Zhao X 2014 *Chin. Phys. B* **23** 098102
[17] Xie Z C, Gao T H, Guo X T and Xie Q 2015 *Comput. Mater. Sci.* **98** 245
[18] Li P T, Yang Y Q, Xia Z H, Luo X, Jin N, Gao Y and Liu G 2017 *RSC Adv.* **7** 48315
[19] Pei Q X, Lu C and Fu M W 2004 *J. Phys.: Condens. Matter.* **16** 4203
[20] Shimono M and Onodera H 2001 *J. Mater. Sci. Eng. A* **304–306** 515
[21] Appel F, Brossmann U and Christoph U 2000 *Adv. Eng. Mater.* **2** 699
[22] Honeycutt J D and Andersen H C 1987 *J. Phys. Chem.* **91** 4950
[23] Stukowski A, Bulatov V V and Arsenlis A 2012 *Modell. Simul. Mater. Sci. Eng.* **20** 085007
[24] Montealegre-Meléndez I, Arévalo C, Pérez-Soriano E, M, Kitzmantel M and Neubauer E 2018 *Metals* **8** 367
[25] Li P T, Yang Y Q, Zhang W, Luo X, Jin N and Liu G 2016 *RSC Adv.* **6** 54763
[26] Yoo M H and Fu C L 1998 *Metall. Mater. Trans. A* **29** 49
[27] Qi Y M. Zhao M and Feng M L J 2021 *Alloys Compd.* **851** 156923
[28] Kishida K, Inui H and Yamaguchi M 1998 *Philos. Mag.* **78** 1